RESEARCH ACTIVITIES VI
Department of Vacuum UV Photoscience

VI-A Electronic Structure and Decay Mechanism of Inner-Shell Excited Molecules

In this project, we have two major subjects: (a) resonant photoelectron spectroscopy and (b) resonant inelastic soft X-ray emission spectroscopy following inner-shell excitations of simple molecules and clusters. We have recently succeeded in development of a next-generation soft X-ray emission spectrometer.

VI-A-1 Improvement of the Energy Resolution of Transmission Grating Soft X-Ray Emission Spectrometer

HATSUI, Takaki; HORIGOME, Toshio; KOSUGI, Nobuhiro

Last year we reported the first results on the performance of a transmission-grating spectrometer (TGS) for high-resolution soft X-ray emission studies. The obtained energy resolution ($E/\Delta E$) was about 3100 at the photon energy of 110 eV, which was limited by the source size on the sample. In order to obtain higher energy resolution, an UHV-compatible entrance slit with the slit opening of 1–30 μm has been developed. The slit blades are mounted on a flexure guided stage in combination with a piezo actuator. The slit opening is feedback controlled by monitoring a capacitance sensor attached to the frame. The performance of the TGS was evaluated by introducing the new entrance slit. The elastic x-ray scattering from aluminum sample irradiated by the monochromatic x-rays (Figure 1) indicates that the overall energy resolution is now 4500 at the photon energy of 114 eV. The resolution is limited by the energy resolving power of the beamline BL3U for the incident soft x-ray, not by the TGS.
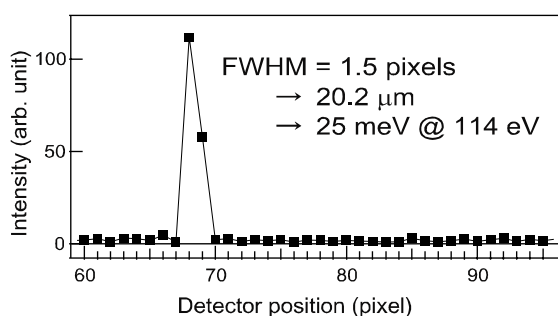
Figure 1. Line profile along dispersion direction of the CCD detector image. Full width at half maximum (FWHM) is 20.2 μm, corresponding to energy resolution of 25 meV ($E/\Delta E$ = 4500).

VI-A-2 Development of a Sub-Pixel Resolution CCD for High Resolution Soft X-Ray Emission Spectrometer

HATSUI, Takaki; HOLLAND, Andrew[1]; INGLEY, Richard[1]; HOLLAND, Karen[2]; KOSUGI, Nobuhiro

(*[1]Brunel Univ.; [2]XCam Ltd.*)

Last year we reported the performance of a transmission-grating spectrometer (TGS) for high-resolution soft X-ray emission studies. The TGS equipped with a conventional charge coupled device (CCD) detector with the pixel size of 13 μm realized an energy resolution $E/\Delta E$ up to 4500 at the photon energy of 114 eV. The observed peak has the full width at half maximum (FWHM) of 1.5 pixels under this high energy-resolution condition. The performance is hence limited dominantly by the spatial resolution of the CCD detector. In order to improve the spatial resolution of the detector, we have developed an electron multiplying CCD detection system with the pixel size of 16 μm for photon-counting detection of the soft x-rays. By amplifying the charge generated by soft x-ray photon prior to on-chip MOSFET, which is the dominant source of the readout noise, the noise is reduced less than 1 electron rms/pixel at the readout rate as high as 400 kHz/pixel. The obtained signals are analyzed to obtain the centroid of the charge, or the position of the x-ray absorption. By examining the image of a slit with a width of 10 μm (Figure 1) and assuming Gaussian profile of the point spread function (PSF) of the detector, the PSF is estimated to have FWHM of 3.0 μm. The results indicate that this new detection technique improves the special resolution by a factor of 10 compared with the conventional CCD detector without degrading the quantum efficiency.
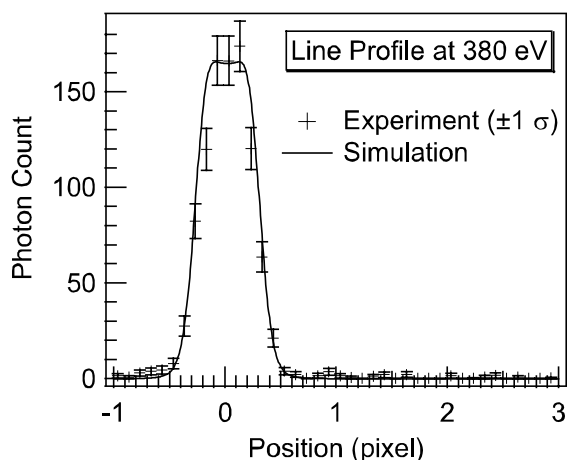
Figure 1. Line profile measured for the image of the slit and simulated profile, based on the diffraction theory assuming the detector PSF with FWHM of 3.0 μm.

VI-B Soft X-Ray Photoelectron-Photoabsorption Spectroscopy and Electronic Structure of Molecular Solids and Clusters

This project has been carried out in international collaboration. We have two subprojects: (a) molecules and radicals in condensed phase and in rare gas matrix, and (b) ionic fragmentation and photoelectron emission of atomic and molecular clusters following the inner-shell resonance excitation. In (a), we have measured excitation spectra in some matrix phases at the bending-magnet beamline BL4B of the UVSOR facility. In (b), we have measured soft X-ray photoelectron spectra of some atomic and molecular clusters on the undulator beamline BL3U.

VI-B-1 Orbital-Dependent Stabilization in the Valence Ionization of CS_2 Cluster

HATSUI, Takaki; PLENGE, Jürgen; RÜHL, Eckart; KOSUGI, Nobuhiro
(*[1]Freie Univ. Berlin*)

Van der Waals clusters have been interested since they give opportunities to investigate the connection between isolated and condensed phases. Cluster formation is known to give the decrease or red shift in adiabatic and vertical ionization (binding) energies, which is commonly interpreted in terms of final-state polarization stabilization. The polarization stabilization is dependent on the distance to the surrounding atoms/molecules and their polarizabilities and numbers.

In the present work, we have investigated red shift dependent on the ionized state of CS_2. Figure 1 shows the spectrum measured by using the He I source, as plotted in relative energy scale, where zero energy is chosen to be the vertical energy of each ionized state of a single molecule. The band profile of the cluster spectrum indicates the abundance or size of the cluster. In the case of larger cluster size with increased stagnation pressure, the peak tops of the cluster bands show larger red shifts. The peak position can be regarded as the vertical binding energy at an average cluster size. We can assume that the vibrational progression of each ionized states does not change upon the cluster formation and is mainly determined by the intra-molecular potentials.

Figure 1 and Table 1 show that the relative binding energies are increased in order of X, A, B, and C. Charge distributions determined by a least-square fitting of the electrostatic potential evaluated by an ab initio MR-SDCI solution for each ionized state of a molecule explain different red shifts. The theoretical charge distribution of a single molecule reasonably predicts that the higher ionized state should have larger polarization stabilization by the surrounding molecules in the cluster.

Figure 1. Valence bands for CS_2 clusters relative to the vertical binding energy of the corresponding state in a molecule.

Table 1. Charge Distribution of a CS_2 molecule in ground and ionized states.

State	Charge O	Charge S	Binding Energy (eV) Theory	Binding Energy (eV) Exp.
Ground state	−0.258	+0.129		
X $^2\Pi_g$	−0.228	+0.614	9.65	10.06
A $^2\Pi_u$	+0.048	+0.476	12.99	12.83
B $^2\Sigma_u^+$	−0.598	+0.799	14.45	14.42
C $^2\Sigma_g^+$	−0.552	+0.776	16.56	16.19

VI-B-2 Absence of Symmetry Breaking Observed for O 1s Core-Excited SO_2 Molecule

LINDGREN, Andreas[1]; KOSUGI, Nobuhiro; GISSELBRECHT, Mathieu[1]; KIVIMÄKI, Antti[1]; BURMEISTER, Florian[2]; NAVES de BRITO, Arnaldo[3]; SORENSEN, Stacey[1]
(*[1]Lund Univ.; [2]Uppsala Univ.; [3]LNLS*)

Electron-ion-ion coincidence measurements of sulphur dioxide at discrete resonances near the O 1*s* ionization edge were carried out. The spectra are analyzed using a dynamic model based upon molecular symmetry and on the geometry of the molecule. We have found clear evidence for molecular alignment which can be ascribed to symmetry properties of the ground and core excited states. Ab initio MR-SDCI calculations indicate geometry changes in accord with the analysis of the measured coincidence spectra. For the SO_2 molecule, however, we have found that the core-hole does not produce measurable evidence for localization, in contrast to the case of ozone, O_3. The dissociation behavior calculated using symmetry-adapted orbitals is equivalent to the behavior derived using symmetry-broken orbitals.

VI-B-3 Radiation Damage Effects on the Electronic Structure of Glycine

MacNAUGHTON, Janay[1]; MOEWES, Alexander[1]; WILKS, Regan[1]; KOSUGI, Nobuhiro
(*[1]Univ. Saskatchewan*)

The emerging field of molecular electronics has focused research on the electronic structures of bio-materials. Soft X-ray absorption and emission spectroscopy are synchrotron-based experimental probes of the electronic states of a material. These techniques can be used to determine structural, electronic and magnetic properties. However, large biological molecules such as proteins and DNA are prone to radiation damage and understanding the mechanisms that lead to the damage is essential. Amino acids are the building blocks of proteins and their simplicity makes them ideal candidates to study the effects of radiation. Radiation damage can cause organic molecules to undergo both structural changes and chemical modifications. Ab initio STEX calculation has been carried out to gain insight into the spectral changes that occur after amino acids are irradiated. It is found that deprotonation is a possible change occurring during the irradiation of glycine with soft X-rays.

VI-C Molecules in Few-Cycle Intense Laser Fields

When the intensity of a laser field reaches as large as ~10^{15} W/cm^2, the magnitude of the electric field component becomes comparable with that of the Coulomb field within a molecule. Thus, the electrons bound in a molecule become heavily perturbed by the external electric field to form a new class of states, often referred to as light-dressed states. Since an internuclear potential within a molecule is deformed in response to the temporal variation of the amplitude of the light field, dynamical processes of molecules such as vibration and chemical bond breaking should be controlled if the light field is properly designed. In the present study, we employed extremely short intense laser pulses with the duration less than 10 fs, to clarify the behavior of molecules through the three-dimensional momentum measurements of the fragment ions produced from a single parent ion.

VI-C-1 Electronic and Nuclear Responses of Fixed-in-Space H$_2$S in Ultrashort Intense Laser Fields

HISHIKAWA, Akiyoshi[1]; TAKAHASHI, Eiji J.; MATSUDA, Akitaka
([1]IMS and JST/PRESTO)

The Coulomb explosion dynamics in non-resonant, ultrashort intense laser fields (12 fs, ~10^{14} W/cm^2) is studied for H$_2$S with its orientation fixed in space, to clarify how the electronic and nuclear responses change by the direction of laser polarization direction (ε) in the molecular frame. The momenta of the respective fragment ions, p_1(H$^+$), p_2(H$^+$) and p_3(S$^+$) produced in the Coulomb explosion process, H$_2$S^{3+} → H$^+$ + S$^+$ + H$^+$, were determined as three-dimensional vectors in the laboratory frame. The kinetic energy release (E_{kin}) and momentum angle (θ_{12}) distributions obtained for the respective directions revealed that the geometrical structure is almost frozen during the interaction with the laser fields for x//ε, while it becomes elongated along the laser polarization vector when ε is parallel to the y- or z-axis, demonstrating that the Coulomb explosion dynamics of H$_2$S in intense laser fields can be manipulated by the polarization direction in the molecular frame.
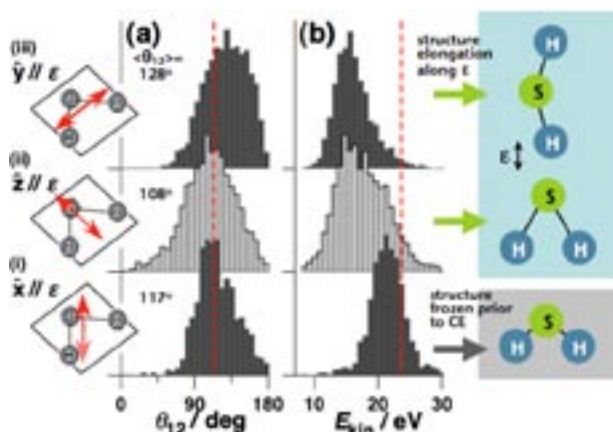
Figure 1. (a) Momentum angle θ_{12} distribution and (b) total kinetic energy E_{kin} distribution obtained for three different directions of ε in the molecular frame, (i) x//ε, (ii) z//ε and (iii) y//ε. Each distribution is normalized at the peak. The dotted lines indicate the θ_{12} and E_{kin} values obtained by a classical simulation of the Coulomb explosion on the *ab initio* PES, θ_{12} = 113.6° and E_{kin} = 23.6 eV, which are smaller than those expected from the corresponding Coulombic PES, θ_{12} = 124.1° and E_{kin} = 29.2 eV.

VI-C-2 Coulomb Explosion Imaging of Molecular Structures with Ultrashort Intense Laser Pulses

HISHIKAWA, Akiyoshi[1]; TAKAHASHI, Eiji J.; MATSUDA, Akitaka
([1]IMS and JST/PRESTO)

The Coulomb explosion process of CS$_2$ in ultrashort (<10 fs) intense laser field (>10^{15} W/cm^2) is investigated. At the field intensity of 5 × 10^{15} W/cm^2, six different symmetric pathways are identified in the Coulomb explosion of CS$_2$, CS$_2^{z+}$ → S^{p+} + C^{q+} + S^{r+}; (p,q,r) = (1,1,1), (1,2,1), (2,1,2), (2,2,2), (3,2,3), (4,2,4) by the coincidence momentum imaging. A good agreement between the results obtained for the (4,2,4) pathway and the momentum distribution expected from the geometry of neutral CS$_2$ was obtained, indicating that the molecular structure is directly reflected in the momentum distribution when fragment ions from highly charged parent ions are monitored.

VI-D Synchrotron Radiation Stimulated High-Speed Etching on Silicon Surfaces

Synchrotron radiation (SR) stimulated process (etching, CVD) has excellent characteristics of unique material selectivity, low damage, low contamination, high spatial resolution and high precision, *etc*. We have utilized these advantages for silicon and silicon oxide substrates fabrication for bio-sensing devices. However, the slow etching rate in the SR-stimulated etching process is the bottle-neck for the through-hole type device fabrication. In this project, we are constructing a new SR-etching system using XeF_2 gas as a etching gas, in order to achieve high-speed SR-etching.

VI-D-1 Construction of High-Speed Synchrotron Radiation Etching System Using XeF_2

NAKAI, Naohito[1]; CHIANG, Tsung-Yi; UNO, Hidetaka; TERO, Ryugo; SUZUI, Mitsukazu; TERAOKA, Yuden[2]; YOSHIGOE, Akitaka[2]; MAKIMURA, Tetsuya[3]; MURAKAMI, Kouichi[3]; URISU, Tsuneo
(*[1]SOKENDAI; [2]JAEA; [3]Univ. Tsukuba*)

We have been constructing a new synchrotron radiation (SR) induced high-speed etching system to make a through-hole type biosensor on Si substrates. The conventional SR-etching using SF_6 has the etching rate of only ~2 nm min^{-1} (at 200 mA ring-current), therefore is not suitable for micrometer-order deep etching. XeF_2 is known as an etching gas for the high-speed vapor-phase etching and is used in the MEMS and µTAS fields. XeF_2 etching has, however, several disadvantages such as; an isotropic etching without directivity; material limitation, for example SiO_2 can not be etched. We expect that SR-induced etching under XeF_2 leads to the high-speed etching with good directivity. We constructed a new etching chamber with LiF window (Figure 1a), and equipped it to the UVSOR-BL4A1. The diagonal mirrors in the beam line will be adjusted to cut off the Li absorption band.
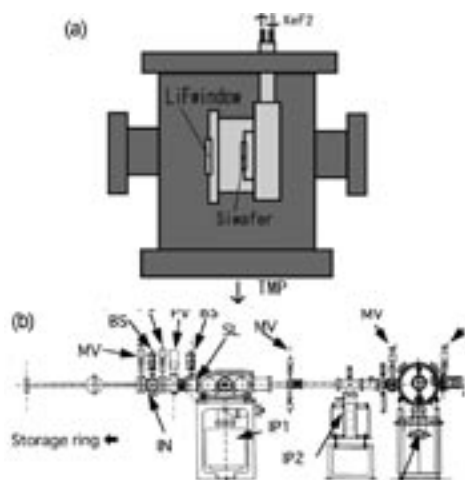
Figure 1. Schematic drawings of (a) the SR-induced XeF_2 etching chamber, and (b) the beam line equipped with the chamber (a).

VI-D-2 Vapor-Phase Etching of Silicon Substrates Using XeF_2

CHIANG, Tsung-Yi; NAKAI, Naohito[1]; UNO, Hidetaka; TERO, Ryugo; SUZUI, Mitsukazu; TERAOKA, Yuden[2]; YOSHIGOE, Akitaka[2]; MAKIMURA, Tetsuya[3]; MURAKAMI, Kouichi[3]; URISU, Tsuneo
(*[1]SOKENDAI; [2]JAEA; [3]Univ. Tsukuba*)

XeF_2 vapor etching without SR irradiation was performed to check our XeF_2 flow system. Test pattern of a photoregist (N-HC600) was deposited on a Si substrate, and exposed to the 300 Pa of XeF_2 for 10–120 min. Figure 1a is the SEM image of the Si substrate after the photoregist removal. The image clearly shows that isotropic etching by XeF_2 has proceeded. Figure 1b shows the line profile of the line-and space pattern with 50 µm width after the XeF_2 etching, measured by a non-contact three-dimensional measurement instrument. The etching rate of 900 nm min^{-1} was obtained.
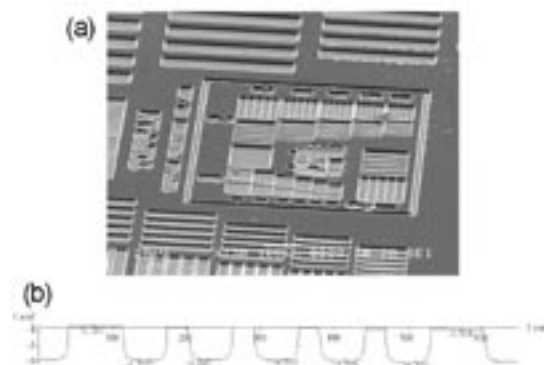
Figure 1. (a) SEM image of the Si substrate after the exposure to 300 Pa of XeF_2 for 10 min. (b) Non-contact three-dimensional measurement profile of the 50 µm wide line-and-space patterns on the Si substrate shown in (a).

VI-E Fabrication of Silicon-Based Planar Ion-Channel Biosensors

It is known that more than 50% of target proteins in the drag discovery field based on the genome information are membrane proteins. The patch clamp method is a powerful and widely used technique for the membrane protein studies, but is not suitable for the high-throughput and multi-integrated screening application. In this project, we have constructed a through-hole silicon device for the ion-channel biosensors. We succeeded to fabricate low-noise planer-type silicon device, and to detect the single ion channel current of gramicidin A.

VI-E-1 Fabrication of Circular Through-Hole on Si(100)-SOI Substrate

ZHANG, Zhen-Long[1]; UNO, Hidetaka; CHIANG, Tsung-Yi; ASANO, Toshifumi[1]; SUZUI, Mitsukazu; TERO, Ryugo; NAKAO, Satoshi; URISU, Tsuneo
(*[1]SOKENDAI*)

We have fabricated a circular through-hole on Si(100)-SOI substrate for channel current measurement. The through-hole is necessary for the electronic conduction, and the circular hole with sharp edge is important for the lipid bilayer membrane formation over the hole and the membrane stability. Figure 1 shows the substrate fabrication process. The Si (100)-SOI (600 µm thick) (Figure 1a) substrate was annealed at water-saturated O_2 flow at 950 °C for 2 h to form a 200 nm thick thermally oxidized layer (Figure 1b). A circular hole with depth of ~550 µm was made by a diamond grinder on the backside surface of the Si(100)-SOI (Figure 1c). Then the hole was etched in tetramethyl ammonium hydroxide (TMAH) until the hole reached to the oxide layer in SOI (Figure 1d). After a 20 nm thick SiO_2 layer was deposited on the top-side surface by sputtering (Figure 1e), the 2–3 µm thick $SiO_2/Si(100)$ layer was penetrated by focused ion beam (FIB) (Figure 1f). The diameter of the hole can be controlled in the range of 1–100 µm. Figure 2 shows the optical microscope image of the through-hole with 100 µm diameter. The through-hole made by the processes shown in Figure 1 had a perfect circular shape and a shape edge.
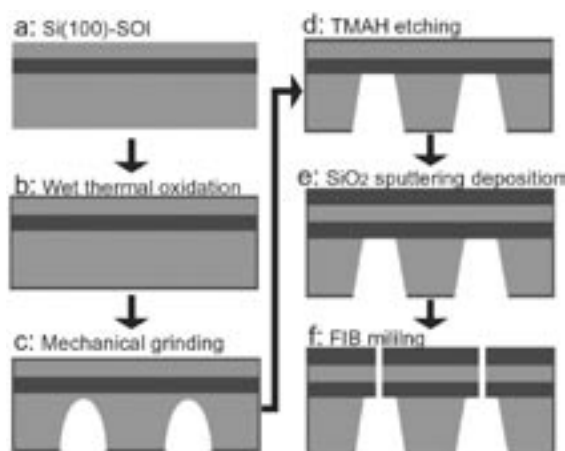
Figure 1. Schematic drawings of the through-hole fabrication processes on a Si(100)-SOI substrate.
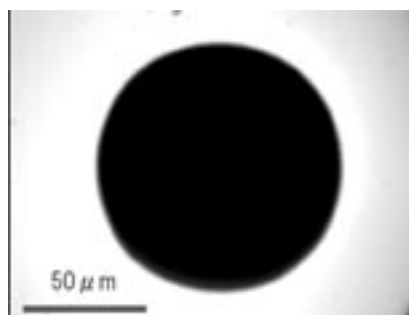
Figure 2. Optical microscope image of the through-hole with 100 µm diameter made by the processes shown Figure 1.

VI-E-2 Channel Current Measurement Using Silicon-Based Planar Type Biosensor

UNO, Hidetaka; ZHANG, Zhen-Long[1]; ASANO, Toshifumi[1]; CHIANG, Tsung-Yi; SUZUI, Mitsukazu; TERO, Ryugo; NAKAO, Satoshi; NONOGAKI, Youichi; URISU, Tsuneo
(*[1]SOKENDAI*)

We have formed a suspended phospholipid bilayer membrane on the Si(100)-SOI through-hole chip (Figure 1), and measured the channel current of gramicidin A (gA). We deposited octadecyltrimethoxysilane by chemical vapor deposition to make the oxidized layer surface of the chip hydrophobic. The through-hole chip was settled in a home-build Teflon chamber, and the suspended bilayer of diphytanoylphosphatidylcholine (DøPC) was formed in the hole by painting method using 10 mg/ml of DøPC/decane solution. The electrical property of the bilayer membrane was measured by a patch clamp amplifier (CEA-2400, Nihon Koden, Japan). Aqueous gA solution was added to the both sides of the bilayer, to reconstitute the gA in to the bilayer. We succeeded in measuring the single channel current of gA using the through-hole silicon chip (Figure 2). Each of the step-signal in Figure 2 is the single channel current thorough gA.
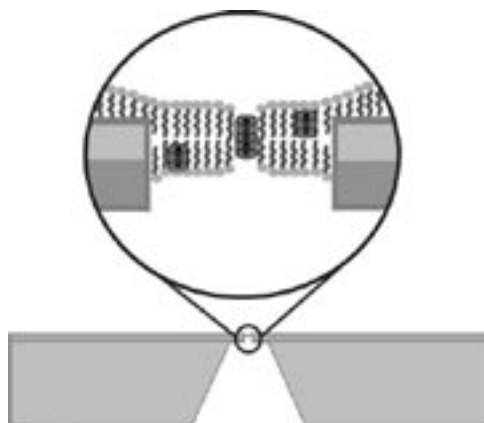
Figure 1. Schematic drawing of the through-hole silicon chip and the suspended lipid bilayer containing gA in the hole.
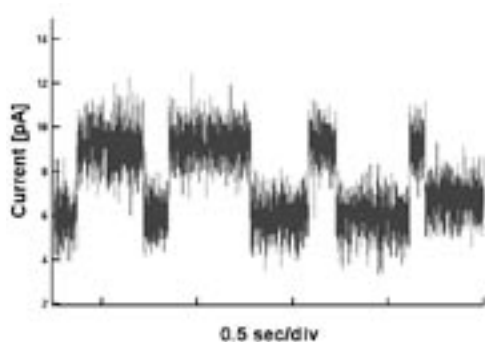
Figure 2. Single ion channel current signals of gA measured by the through-hole silicon chip. Bias voltage is 150 mV.

VI-E-3 Noise Analysis in the Planar-Type Ion-Channel Biosensors

UNO, Hidetaka; ZHANG, Zhen-Long[1]; CHIANG, Tsung-Yi; SUZUI, Mitsukazu; TERO, Ryugo; NAKAO, Satoshi; NONOGAKI, Youichi; URISU, Tsuneo
(*[1]SOKENDAI*)

Low noise electronic systems in pA order is necessary for the ion channel current detection from single molecule. It has been believed that silicon is an inept material in ion channel detecting, because its high dielectric loss causes high noise level. However, our through-hole silicon chip during the gA channel measurement showed sufficiently low noise level (1.7 pA, rms). We investigated the noise sources in our silicon chip based on the dimension parameters shown in Figure 1. The main noise sources in planar bilayer recordings are; (1) I_h: the current noise from the interaction between the head-stage input voltage noise (e_n) and the input capacitance (C_t); (2) I_{Ra}: the current noise due to the thermal voltage noise of the access resistance R_a in series with the bilayer capacitance C_m; (3) I_d: the dielectric noise. These noise variances are expressed as

$$I_h^2 = (4/3)e_n^2 \pi^2 C_t^2 B^3 \tag{1},$$
$$I_{Ra}^2 = (4/3)k\,T\,R_a\,(2\pi\,C_m)^2\,B^3 \tag{2},$$
$$I_d^2 = 4k\,T\,\pi\,D\,C_t\,B^2 \tag{3},$$
$$C_t = C_m + C_{sub} + C_{others} \tag{4},$$

where B is the frequency band width, C_{sub} is the capacitance of the substrate, C_{others} is the sum of other capacitances contributing to noise. The measured noise current I_m is given by

$$I^2 = I_h^2 + I_{Ra}^2 + I_d^2 \tag{5}.$$

We calculated these capacitance and noise current values based on the substrate structure used in our experiments shown in Figure 1. The calculated values in B =5 kHz are; C_m = 76 pF; C_{sub} = 2 pF; C_{others} = 1.2 pF; C_t = 80 pF; $I_h^2 = 5.5 \times 10^{-26}$ A^2 (assuming $e_n = 2.3 \times 10^{-9}$ V Hz$^{0.5}$); R_a = 1.7 kΩ; and $I_{Ra}^2 = 2.7 \times 10^{-25}$ A^2. Thus the calculated noise current I = 1.7 pA (rms) was obtained. This value is in quite good agreement with the measured value 1.2 pA. We found that the SiO$_2$ disk around the hole (C$_1$ region in Figure 1) contributed to the low noise level in our chip.
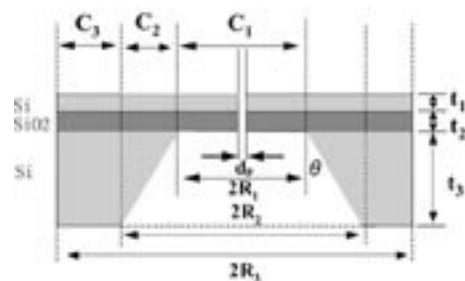
Figure 1. Schematic drawing of the through-hole silicon chip and its dimension parameters.

VI-F Integration and Characterization of Bio-Functional Materials on Silicon Surfaces

Integration of bio-functional materials on solid surfaces is an attractive research theme and important to the development of new biosensors and screening methods in which biological reactions are directly detected on electronic circuits. We have investigated the lipid bilayer membrane deposition and covalent immobilization of protein, and have characterized the properties of these bio-functional materials using atomic force microscopy infrared absorption spectroscopy. We have also developed a new infrared absorption spectroscopy system using buried-metal-layer substrate, for the in-situ measurements of water/solid interface.

VI-F-1 Supported Phospholipid Bilayer Formation on Hydrophilicity-Controlled Silicon Dioxide Surfaces

TERO, Ryugo; WATANABE, Hidekazu[1]; URISU, Tsuneo
(*[1]RIKEN*)

We investigated the influence of surface hydroxyl groups (-OHs) on the supported planar phospholipid bilayer (SPB) formation and characteristic. We prepared SiO_2 surfaces with different hydrophilicity degree by annealing the SiO_2 layer on Si(100) formed by wet chemical treatments. The hydrophilicity reduced with irreversible thermal desorption of -OHs. We formed SPB of dimyristoylphosphatidylcholine (DMPC) on the SiO_2 surfaces by incubation at a 100-nm-filtered vesicle suspension. The formation rate was faster on less hydrophilic surfaces (Figure 1). We proposed that a stable hydrogen-bonded water layer on the SiO_2 surface worked as a barrier to prevent vesicle adhesion on the surface. Theoretical calculation indicates that water molecules on vicinal surface -OHs take a stable surface-unique geometry, which disappears on an isolated -OH. The surface -OH density, however, little affected the fluidity of once formed SPBs, which was measured by the fluorescence recovery after photobleaching method. We also describe about the area-selective SPB deposition using surface patterning by the focused ion beam.
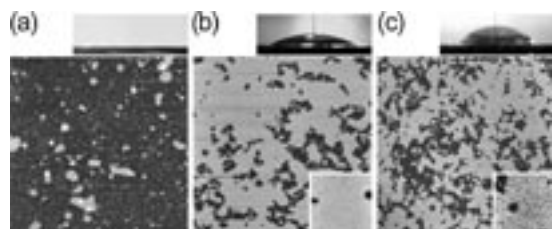
Figure 1. AFM images of DMPC-SPB on hydrophilicity-controlled SiO_2/Si(100) surfaces. The water contact angle of the SiO_2 surfaces before the DMPC deposition and the SPB coverage are; (a) 5°, 0.12; (b) 24°, 0.78; and (c) 67°, 0.67, respectively. The AFM images were obtained in a buffer solution.

VI-F-2 Orientation of Avidin Molecules Immobilized on COOH-Modified SiO_2/Si(100) Surfaces

MISAWA, Nobuo; YAMAMURA, Shusaku[1]; KIM, Yong-Hoon[1]; TERO, Ryugo; NONOGAKI, Youichi; URISU, Tsuneo
(*[1]SOKENDAI*)

Avidin molecules were immobilized on a COOH-modified SiO_2/Si(100) surface with sub-nanometer order flatness (root-mean-square (rms) roughness ~0.1 nm) forming covalent bonds between the COOH groups on the substrate surface and the NH_2 groups of avidin molecules. The structures of avidin-immobilized sur-faces were investigated by atomic force microscopy (AFM), ellipsometry, and infrared (IR) reflection absorption spectroscopy using buried metal layer substrate (BML-IRRAS), and transmission IR absorption spectroscopy (TIRAS). We have simulated dependence of the amide I band intensity on the avidin orientation (Figure 1), since BML-IRRAS and TIRAS are sensitive to perpendicular and parallel dipole moments to the surface, respectively. These data have evidenced that the avidin molecules are immobilized with the 2-fold symmetry axis of the tetramer almost perpendicularly to the substrate surface.
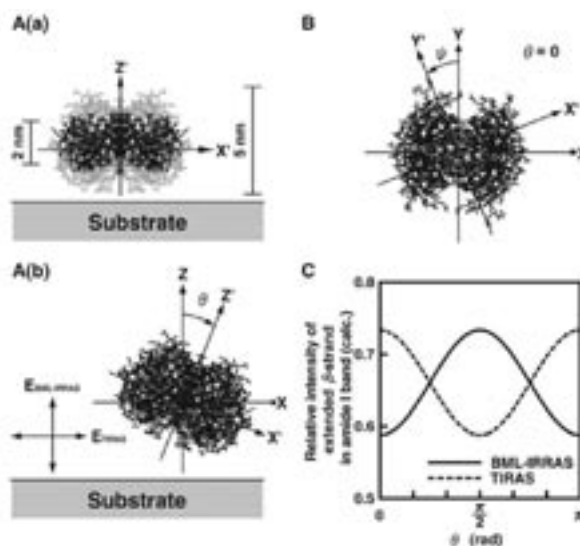
Figure 1. Schematic images of an egg white avidin molecule immobilized on the substrate surface. All component atoms are plotted using the coordinate data given in PDB (1AVD) as dots of the same size in A(a): avidin tetramer (gray) and the only β-barrel part (dark). Coordinates *X*, *Y* and *Z* are fixed to the substrate surface, while *X'*, *Y'* and *Z'* are fixed to the molecule. Molecular orientation is defined by the Eulerian angles, φ (= 0), θ and ψ in A(b) and B. Electric fields, $E_{BML-IRRAS}$ and E_{TIRAS}, in BMLIRRAS and TIRAS are drawn in A(b). Calculated relative intensities of extended b-strand peak in the amide I band as a function of θ ($0 \leq h \leq \pi$) are shown in C.

VI-F-3 AFM Characterization of Gramicidin-A in Tethered Lipid Membrane on Silicon Surface

LEI, Sheng-Bin[1]; TERO, Ryugo; MISAWA, Nobuo; YAMAMURA, Shusaku[2]; WAN, Li-Jun[1]; URISU, Tsuneo
(*[1]IMS and Chinese Acad. Sci.; [2]SOKENDAI*)

The tethered 1,2-dipalmitoyl-*sn*-glycero-3-phosphocholine (DPPC) lipid bilayer is formed on the oxidized Si surfaces using the avidin-biotin interaction to investigate the lipid-membrane protein interactions by using gramicidin-A (g-A) as a model membrane protein. The morphology of the tethered lipid bilayer, observed by the *in situ* atomic force microscopy (AFM), changes drastically by the reconstruction of g-A (Figure 1). The aggregation behavior of g-A is clearly different in the tethered membrane from those in the simple supported

membranes on mica and SiO$_2$ surfaces. The thick water layer under the membrane introduced by the tethered structure gives important influence on the aggregation behavior of g-A.
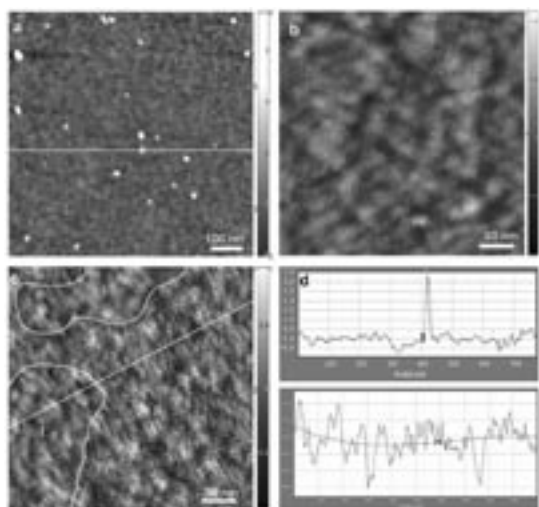
Figure 1. Topography images of (a) avidin immobilized substrate, and tethered lipid bilayers (b) without and (c) with 1 mol% g-A. (d) The line profile of marked place in (a) and (c). Color scales are (a) 7.5 nm, (b) 1.7 nm and (c) 1.5 nm full scale.

Figure 1. (a) Schematic drawings of the sample holder for the new BML-IRRAS system. (b) IR power spectra measured by the new BML-IRRAS instrument for (a) air, (b) D$_2$O and (c) H$_2$O with 12 nm thickness.

VI-F-4 In-Situ Infrared Reflection Absorption Spectroscopy System Using Buried Metal Layer Substrate (BML-IRRAS) for Biomaterials under Water

SAYED, Md. Abu[1]; UNO, Hidetaka; MISAWA, Nobuo; HARADA, Kensuke[2]; TANAKA, Keiichi[2]; KONDOH, Takuhiko; TERO, Ryugo; URISU, Tsuneo
(*[1]SOKENDAI; [2]Kyushu Univ.*)

Supported membrane on biosensor surface is one of the most attractive research fields in these days. For new bioactive biosensor or biochips for diagnostics or other electronic purposes we have to study biomaterial properties on solid surfaces in different conditions. Many experimental approaches including infrared reflection absorption spectroscopy using buried metal layer (BML-IRRAS) have been performed to study the function of biomaterials on inorganic surfaces. But there are few IRRAS techniques to study the membrane surface reaction under aqueous solution. We have constructed a new BML-IRRAS system to study biomaterials under water. We used CaF$_2$ prism and 12 µm aluminum spacer upon BML substrate including a solution injection system (Figure 1a). We used JIR-7000 (JEOL Ltd.) with a MCT detector as a FT-IR system. Although water is necessary for biomaterials to keep life functions, but water have strong absorptivity in the IR region. We have investigated the window regions for H$_2$O and D$_2$O as shown in Figure 1b. It is concluded that 1250–4000 cm^{-1} and 3700–4000 cm^{-1} are applicable for IR measurements in D$_2$O and H$_2$O, respectively, in the present system.

VI-G Extreme UV Photoionization Studies of Fullerenes by Using a Grazing-Incidence Monochromator and High-Temperature Mass Spectrometer

On the beam line BL2B in UVSOR a grazing incidence monochromator has been constructed which supplies photons in the energy region from 20 to 200 eV [M. Ono, H. Yoshida, H. Hattori and K. Mitsuke, *Nucl. Instrum. Methods Phys. Res., Sect. A* **467-468**, 577–580 (2001)]. This monochromator was assumed to bridge the energy gap between the beam lines BL3B and BL4B, thus providing for an accelerating demand for the high-resolution and high-flux photon beam from the research fields of photoexcitation of inner-valence electrons, *L*-shell electrons in the third-row atom, and $4d$ electrons of the lanthanides.

Since 2001 we have tried taking photoion yield curves of fullerenes. Geometrical structures and electronic properties of fullerenes have attracted widespread attention because of their novel structures, novel reactivity, and novel catalytic behaviors as typical nanometer-size materials. Moreover, it has been emphasized that the potential for the development of fullerenes to superconductors ($T_c \sim 50$ K) and strong ferromagnetic substances is extremely high. In spite of such important species spectroscopic information is very limited in the extreme UV region, which has been probably due to difficulties in obtaining enough amount of sample. The situation has rapidly changed in these few years, since the techniques of syntheses, isolation, and purification have been advanced so rapidly that appreciable amount of fullerenes is obtainable from several distributors in Japan.

VI-G-1 Refinements of the Estimation of Photoabsorption Cross Sections of Metallofullerenes

KATAYANAGI, Hideki; PRODHAN, Md. Serajul Islam[1]; MITSUKE, Koichiro
(*[1]SOKENDAI*)

We have revisited the photoabsorption cross sections of endohedral metallofullerenes ($Ce@C_{82}$, $Dy@C_{82}$ and $Pr@C_{82}$) in the extreme ultraviolet[1–3] and refined the procedure of their precise estimation. In the previous studies the cross sections were evaluated by comparing normalized count rates for the metallofullerenes with those for a standard sample. The cross sections thus obtained are found to serve as only crude approximations, since no consideration was given to the detection efficiency dependence of the time-of-flight mass spectrometer on sample masses and charges.

In the present study, we adopted an alternative approach to obtain more precise cross sections of the metallofullerenes. First, multiple standard samples having different masses were utilized for correction of the detection efficiency dependence. Second, such corrections were made by applying an empirical formula proposed by Twerenbold *et al.*[4] Table 1 summarizes refined partial photofragmentation cross sections of $Pr@C_{82}$ and its total photoabsorption cross sections. All these values are the means of the two cross sections that were calculated using xenon and C_{60} as standard samples. The deviations of the values in Table 1 are at most 12%, which implies that the detection efficiency dependence is fairly corrected. Indeed, the total photoabsorption cross section of 36 Mb at 110 eV is in good agreement with that of 82 carbon atoms, 33.5 Mb. Refinements of the cross sections of other metallofullerenes using several standard samples are also in progress.

References
1) K. Mitsuke, T. Mori, J. Kou, Y. Haruyama and Y. Kubozono, *J. Chem. Phys.* **122**, 064304 (2005).
2) K. Mitsuke, T. Mori, J. Kou, Y. Haruyama, Y. Takabayashi and Y. Kubozono, *Int. J. Mass Spectrom.* **243**, 121 (2005).
3) H. Katayanagi, B. P. Kafle, J. Kou, T. Mori, K. Mitsuke, Y. Takabayashi, E. Kuwahara and Y. Kubozono, *J. Chem. Phys.* submitted.
4) D. Twerenbold, D. Gerber, D. Gritti, Y. Gonin, A. Netuschill, F. Rossel, D. Schenker and J. L. Vuilleumier, *Proteomics* **1**, 66 (2001).

Table 1. Partial photofragmentation cross sections of $Pr@C_{82}$ for the formation of $Pr@C_{82}{}^{z+}$ and the total photoabsorption cross sections at the photon energies of 110 and 130 eV. All cross sections are in Mb.

Photon energy	Photofragmentation cross section		Total cross section
	$Pr@C_{82}{}^{+}$	$Pr@C_{82}{}^{2+}$	
110 eV (off-resonance)	22.2	13.8	36.0
130 eV (on-resonance)	32.7	22.6	55.3

VI-G-2 Fragmentation Mechanism of Highly Excited C_{70} Cations in the Extreme Ultraviolet

MITSUKE, Koichiro; KATAYANAGI, Hideki; KOU, Junkei; MORI, Takanori; KUBOZONO, Yoshihiro[1]
(*[1]Okayama Univ.*)

[*AIP Conf. Proc.* **811**, 161–166 (2006)]

The ion yield curves for $C_{70-2n}{}^{z+}$ ($n = 1–8$, $z = 2$ and 3) produced by photoionization of C_{70} were measured in the photon energy ($h\nu$) range of 25–150 eV. The appearance $h\nu$ values were higher by *ca.* 34 eV than the thermochemical thresholds for dissociative ionization of C_{70} leading to $C_{70-2n}{}^{z+}$ (see Figure 1). Evaluation was made on the upper limits of the internal energies of the primary $C_{70}{}^{z+}$ above which $C_{70-2n+2}{}^{z+}$ fragments cannot escape from further dissociating into $C_{70-2n}{}^{z+} + C_2$. These critical internal energies agreed well with appearance internal energies of $C_{70}{}^{z+}$ theoretically obtained

corresponding to the threshold for the formation of $C_{70-2n}{}^{z+}$. The photofragmentation of the parent $C_{70}{}^{z+}$ ions is considered to be governed by the mechanism of internal conversion of their electronically excited states, statistical redistribution of the excess energy among a number of vibrational modes, and sequential ejection of the C_2 units.
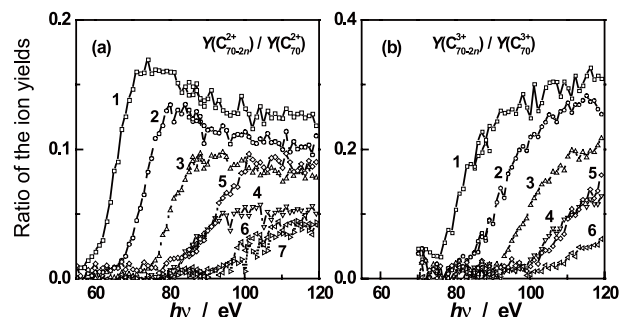
Figure 1. Relative ion yield curves of $C_{70-2n}{}^{z+}$ ions obtained from time-of-flight mass spectra. (a) $z = 2$, $n = 1$–7 and (b) $z = 3$, $n = 1$–6.

VI-H Photoiononization and Fragmentation Mechanisms of C_{60} and C_{70} in the Extreme Ultraviolet

When fullerenes gain enough amount of energy through photoionization processes, primarily formed ions are known to undergo decomposition into fragment ions with even numbered carbon atoms. We have measured the yield curves for $C_{60-2n}{}^{z+}$ from C_{60} as a function of the internal energy E_{int} of the parent $C_{60}{}^{z+}$ ions to study the mechanisms and kinetics of the above unimolecular reactions. These experimental yield curves have been compared with the theoretical fractional abundance curves. We found that the experimental and theoretical curves provide almost the same appearance internal energies for the formation of $C_{60-2n}{}^{z+}$ ($n \geq 1$). This result appears to reveal that the excess energy is statistically distributed among the internal degrees of freedom of the parent ions and that C_2 units are ejected sequentially ($C_{60}{}^{z+} \rightarrow C_{58}{}^{z+} + C_2$, $C_{58}{}^{z+} \rightarrow C_{56}{}^{z+} + C_2$, ..., $C_{60-2n+2}{}^{z+} \rightarrow C_{60-2n}{}^{z+} + C_2$).

There remains ambiguity as to whether potential barrier exists along the reaction coordinate and whether resonant state participates during dissociation. Moreover, a few groups have argued that another mechanism of single-step two-fragment fission ($C_{60}{}^{z+} \rightarrow C_{60-2n}{}^{z+} + C_{2n}$) could be involved in the formation of $C_{60-2n}{}^{z+}$. To elucidate these issues, we are developing two devices which are incorporated into the present photoionization spectrometer for gaseous fullerenes: photofragment imaging analyzer and threshold photoelectron-photoion coincidence apparatus.

VI-H-1 Kinetic Energy Analysis of the Fragment Ions Produced from C_{60} and C_{70}

KATAYANAGI, Hideki; KAFLE, Bhim Prasad[1]; PRODHAN, Md. Serajul Islam[1]; YAGI, Hajime; MITSUKE, Koichiro
(*[1]SOKENDAI*)

We have reported the yield curves[1,2] of the fragments $C_{60-2n}{}^{z+}$ and $C_{70-2n}{}^{z+}$ ($n = 1$, $z = 1$) produced by photoionization of solitary C_{60} and C_{70}, respectively, in the photon energy range of 45–150 eV. Then the mechanism of sequential loss of C_2 units has been proposed on a basis of comparison between the experimental ion yield curves and theoretical fractional abundance curves. The latter curves have been derived by employing the RRKM theory to individual unimolecular reactions, $C_{60-2n+2}{}^{z+} \rightarrow C_{60-2n}{}^{z+} + C_2$. More reliable calculations of the rate constants of the consecutive reactions are needed before closer comparison between the two curves. For such calculations we should know precise values of the activation energies for the reactions, together with the vibrational spectra of the transition states. This induced us to develop a new ion spectrometer for the fragment ions produced from $C_{60}{}^{z+}$ and

$C_{70}{}^{z+}$. It is likely that the magnitude of the potential barriers of the reactions can be estimated from the average kinetic energy release measured by this spectrometer.

References
1) J. Kou, T. Mori, Y. Kubozono and K. Mitsuke, *Phys. Chem. Chem. Phys.* **7**, 119 (2005).
2) K. Mitsuke, H. Katayanagi, J. Kou, T. Mori and Y. Kubozono, *AIP Conf. Proc.* **811**, 161 (2006).

VI-H-2 Photofragment Imaging Apparatus for Measuring Momentum Distributions in Dissociative Photoionization of Fullerenes

KAFLE, Bhim Prasad[1]; PRODHAN, Md. Serajul Islam[1]; KATAYANAGI, Hideki; MITSUKE, Koichiro
(*[1]SOKENDAI*)

[*AIP Conf. Proc.* in press]

We are developing a photofragment imaging apparatus based on time-of-flight (TOF) mass spectrometry to measure the kinetic energy and angular distributions

of the fragments. We have adopted the Eppink–Parker type three-element velocity focusing lens system[1] (electrodes R, E, and T) to achieve high kinetic energy resolution on the photofragment images. Furthermore, we have utilized a potential switcheable mass gate M and an ion reflector G inside the TOF tube as demonstrated in Figure 1, to select a bunch of fragments having the same mass-to-charge ratio m/z from neighboring bunches $(m\pm24)/z$. As long as M is kept grounded, all fragments are reflected back by G and do not impinge against the imaging detector PSD. When an entire bunch of the fragments having an expected m/z arrives inside M, a pulsed voltage is applied there. The potential energies of the ions in this bunch are suddenly elevated, so that these ions can exclusively pass through G and reach the PSD.

For optimizing the dimensions of the setup, we have performed ion trajectory simulations utilizing the SIMION software. We considered that the dissociative ionization of C_{60} takes place within a region of rectangular parallelepiped $\Delta x \Delta y \Delta z = 1\times3\times1$ mm^3 in the ionization region of the spectrometer. The simulated trajectories of C_{60}^+, C_{58}^+ and C_{56}^+ at initial kinetic energy of 0.1 eV show that the trajectories of unwanted C_{60}^+ and C_{56}^+ ions are reflected completely. On the other hand, most of the trajectories of C_{58}^+, the ion whose momentum image we wish to measure, are found to go beyond G and reach the PSD. This observation provides direct evidence for exclusive imaging detection of C_{58}^+.

Reference
1)A. T. J. B. Eppink and D. H. Parker, *Rev. Sci. Instrum.* **68**, 3477 (1997).

Figure 1. Schematic view of the momentum imaging spectrometer and simulated trajectories of C_{58}^+ at initial kinetic energies of 0.1 eV. R, repeller; E, extractor; T, entrance electrode of a time-of-flight drift tube (TOF); IT, Ion trajectories; M, mass gate; G, ion reflector. The dimensions of all the electrodes are determined from the SIMION 3D software.

VI-H-3 Simulated Image of Fragment Ions Produced from C_{60}

KAFLE, Bhim Prasad[1]; PRODHAN, Md. Serajul Islam[1]; YAGI, Hajime; KATAYANAGI, Hideki; MITSUKE, Koichiro
(*[1]SOKENDAI*)

Our photofragment imaging spectrometer under construction is found to realize excellent momentum imaging detection of fullerene fragments with a particular cluster size. To demonstrate its capability, we have reproduced a simulated image of fragment ions C_{58}^+ from C_{60} with different kinetic energies. Figure 1 shows the image of the C_{58}^+ ions on the PSD at the kinetic energies of 0.1 eV (triangles) and 0.11eV (circles). We have taken into account the ion trajectories generated in

the elevation and azimuth angle ranges of 0° to +90° and 0° to +180°, respectively, which cover only one quarter of the full three-dimensional trajectories over the 4π solid angle. The trajectories with a given elevation angle form a horizontal stripe, and the envelope of all the stripes makes an arc. This clearly demonstrates that scattering distribution in spherical symmetry can be successfully projected on an image plane. It is likely that the two images are almost separable if their kinetic energy difference is larger than 0.01 eV. Comparison between the simulations with and without the ion reflector G (see Figure 1 of VI-H-2) confirmed that the images are not distorted in the presence of G. The present momentum imaging spectrometer will be installed at the end station of beam line 2B in the UVSOR facility.
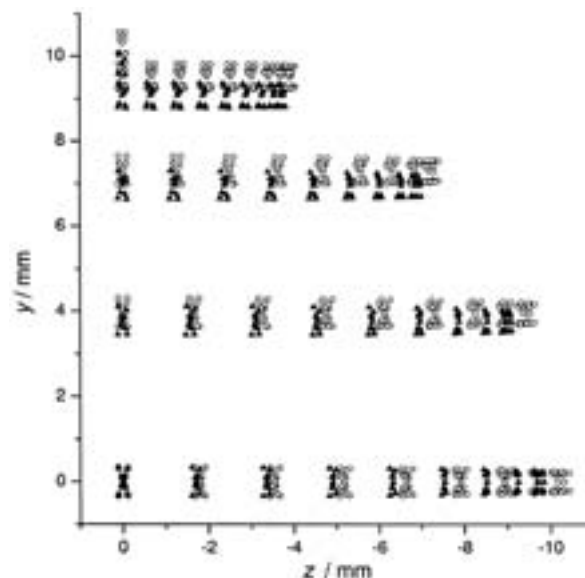
Figure 1. Simulated image of C_{58}^+ ions at the kinetic energies of 0.1 (▲) and 0.11 eV (○). The three-dimensional scattering distribution of the ions is projected on the PSD.

VI-H-4 Scattering Distributions of the Photofragments from C_{60} in the Extreme Ultraviolet

PRODHAN, Md. Serajul Islam[1]; KAFLE, Bhim Prasad[1]; YAGI, Hajime; KATAYANAGI, Hideki; MITSUKE, Koichiro
(*[1]SOKENDAI*)

In thermodynamic equilibrium the velocity distribution of a large number of C_{60} molecules can be represented by the Maxwell-Boltzmann form of

$$f_0(\vec{v}) \;\propto\; \left[\frac{m}{2\pi kT}\right]^{\frac{3}{2}} \exp\left(\frac{-mv^2}{2kT}\right) \qquad (1)$$

where the density and temperature are assumed to be independent of the positions of molecules. Therefore, the velocity distribution of the photofragments from C_{60} in the laboratory system can be expressed as that in the center-of-mass system convoluted with the initial Maxwell-Boltzmann distribution before photoionization. We will perform deconvolution procedure to derive the

velocity distribution in the center-of-mass system, which is needed to decide on a dominant mechanism in fragmentation of electronically excited C_{60} cations, from the three-dimensional velocity distributions of the fragment ions measured by using our imaging spectrometer.

VI-H-5 Why We Wish to Measure the Yield Curves of the Photofragments from C_{60} in Coincidence with Threshold Electrons

MITSUKE, Koichiro; KATAYANAGI, Hideki; KAFLE, Bhim Prasad[1]; PRODHAN, Md. Serajul Islam[1]; YAGI, Hajime
(*[1]SOKENDAI*)

We have derived the E_{int}-dependence of the C_{60-2n}^{z+} yield from the experimental $h\nu$-dependent yield, and then compared the former dependence with the theoretical fractional abundance near the onset region.[1] Such a comparison may become less meaningful further away from the onset region. This is because, in our estimate of E_{int} of the primary C_{60}^{z+}, we have disregarded the energy transmission from a portion of $h\nu$ to the photoelectron kinetic energy, and eventually substantial errors have been produced in the E_{int}-dependence curve. To convert the $h\nu$-dependent yield accurately to the E_{int}-dependence, we require the partial photoionization cross section of C_{60} for the formation of C_{60}^{z+} as a function of both $h\nu$ and E_{int}. However, it is far from easy to obtain the partial photoionization cross section in wide $h\nu$ and E_{int} ranges from conventional two-dimensional photoelectron spectroscopy. Thus we are planning to measure (a) the yield curve of threshold electrons and (b) that of C_{60-2n}^{z+} *in coincidence with* the threshold electrons. Using these two curves we will be able to calculate a proper E_{int}-dependence of the C_{60-2n}^{z+} yield.

Reference
1) K. Mitsuke, H. Katayanagi, J. Kou, T. Mori and Y. Kubozono, *AIP Conf. Proc.* **811**, 161 (2006).

VI-H-6 ZEKE Photoelectron Spectroscopy Utilizing the Dark Gap of UVSOR Storage Ring

KATAYANAGI, Hideki; KAFLE, Bhim Prasad[1]; PRODHAN, Md. Serajul Islam[1]; YAGI, Hajime; MITSUKE, Koichiro
(*[1]SOKENDAI*)

Last year we constructed a threshold photoelectron spectrometer for the purpose of measuring the signal of threshold electron-photoion coincidence (TEPICO), using the dark gap of the synchrotron radiation facility. Such measurements provide us with the detailed information about the excitation/dexication and decay processes of gaseous fullerenes (C_{60} and C_{70}). We already succeeded in observing the threshold electron signal using He and O_2 samples, but the spectra suffered from intense background counts. The background needs to be reduced to the utmost for performing the TEPICO measurement. Also an improvement of the spectrometer in the efficiency for threshold electrons is urgently needed. For these requirements, we are now developing an improved version of the spectrometer which has the capability to significantly reject the electrons with high kinetic energies and to guide electrons with zero or very small kinetic energies (0 to 10 meV) to the detector.

VI-H-7 New Design of a ZEKE Photoelectron Spectrometer for Photofragmentation Studies of Fullerenes

KAFLE, Bhim Prasad[1]; KATAYANAGI, Hideki; MITSUKE, Koichiro
(*[1]SOKENDAI*)

Figure 1 shows a schematic diagram of our improved threshold photoelectorn spectrometer, together with typical trajectories for 10 meV photoelectrons. Here, a voltage of $E_E = 3$ V is applied to the extraction electrode. The extraction and screening electrodes are 1 mm in thickness and central circular apertures of 7 mm in diameter are drilled. The arrangement of the electrodes was optimized by using the SIMION software.[1] We have adopted penetrating field technique which was invented by King and coworkers.[2] In this technique a potential well is formed in the ionization region by the field penetration from the potential of the extraction electrode through the screening electrode, providing a very large solid angle of collection for slow electrons ($\sim 4\pi$ sr). Slow electrons are focused again at a crossover point inside a three-element asymmetric lens system beyond which they can reach the detector. In contrast, high energy electrons are strongly suppressed by the field of the asymmetric lens system. The proportion of the detectable trajectories is determined by simulation as a function of the electron kinetic energy. The results at $E_E = 3$ V are shown in Figure 2.

References
1) D. A. Dahl, SIMION 3D Version 7.0 User's Manual, Idaho falls: 2000.
2) R. I. Hall, A. McConkey, K. Ellis, G. Dawber, L. Avaldi, M. A. MacDonald and G. C. King, *Meas. Sci. Technol.* **3**, 316 (1992).
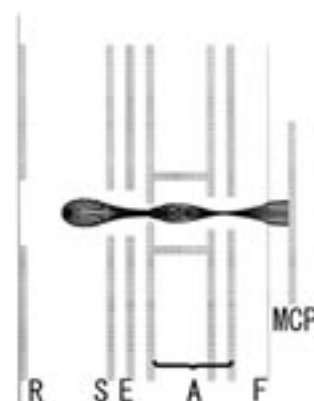
Figure 1. Schematic view of the threshold photoelectron spectrometer and simulated trajectories at the initial kinetic energy of 10 meV. From ionization center 36 electron trajectories were generated in the ejection angle of 0° to 360°, at an interval of 10°. R, repeller; S, screening electrode; E, extraction electrode; A, asymmetric lens system; F, front-plate electrode.
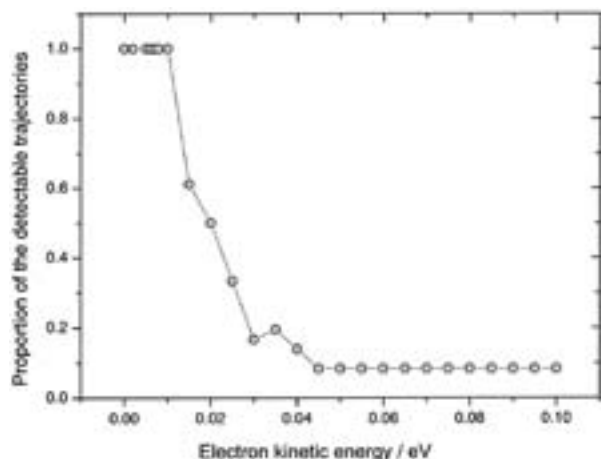
Figure 2. Proportion of the detectable trajectories determined by simulation at E_E = 3 V. The curve shows a sharp increase below 20 meV.

VI-H-8 High Resolution Photoelectron Spectroscopy of Gaseous Fullerenes

YAGI, Hajime; KATAYANAGI, Hideki; KAFLE, Bhim Prasad[1]; PRODHAN, Md. Serajul Islam[1]; MITSUKE, Koichiro
(*[1]SOKENDAI*)

Photoemisson measurements of solitary C_{60} and C_{70} have been made by several groups, but their energy resolution was *ca.* 100 meV at the best. We are developing an apparatus of high-resolution angle-resolved photoemission spectroscopy, using a helium discharge lamp or synchrotron radiation. Our goal is to carry out photoemisson spectroscopy of various kinds of gaseous fullerenes with a total energy resolution of ~20 meV. Fullerenes have a number of degenerated bands within 40 eV from the Fermi energy. Definite assignments of the peaks in the photoemisson spectra of fullerenes are expected to be easier in the gas phase than in the solid phase, since band broadening and interference of secondary electrons are substantially reduced in the gas phase. Some of the peaks arising from excitations to different vibrational states of excited C_{60}^+ ions might be distinguishable. As for metallofullerenes it is documented that electron transfer takes place from the encapsulated metal atoms to the fullerene cages. For instance, valence-band photoemission studies of the La@C_{82} film showed that new peaks due to triply electron transfer emerge near the Fermi energy. Such peaks are expected to be seen more clearly in the gas phase. By measuring the photoion yield curves, we observed for the first time the $4d \rightarrow 4f$ giant dipole resonance in Ce@C_{82} and Pr@C_{82}. Using synchrotron radiation, we will perform resonant photoemission spectroscopy of these species to confirm the presence of giant dipole resonance and to study the dynamics of the $4f$ electrons of encapsulated metal atoms.

VI-H-9 Construction of an End Station of BL2B to Study Dissociative Photoionization of Fullerenes and VUV Spectroscopy of Ionic Liquids

KATAYANAGI, Hideki; KAFLE, Bhim Prasad[1]; PRODHAN, Md. Serajul Islam[1]; YAGI, Hajime; MITSUKE, Koichiro
(*[1]SOKENDAI*)

A new vacuum chamber for the end station of beam line 2B (BL2B) in UVSOR was constructed. The chamber was designed for the gas phase spectroscopy of refractory materials such as fullerenes, metalloencapsulated fullerenes and ionic liquids. The following three subjects are now under way: (1) the velocity map imaging[1] of the ionic photofragments from fullerenes, (2) threshold photoelectron–photoion coincidence measurements of the fullerenes, and (3) photoelectron and photoabsorption spectroscopy of ionic liquids. The installation of the chamber at BL2B was accomplished. We are going to instrument various spectrometers into the chamber for the above experiments.

Drawing of the chamber is shown in Figure 1. The twofold μ-metal shield is put inside the chamber to prevent penetration of the geomagnetic field. The effective volume surrounded by the shield is five times as large as that of the previous chamber used at BL2B. The new chamber is equipped with 14 ports facing the ionization region, *i.e.* the focal point of the synchrotron radiation. This larger volume and versatile port arrangement enable us to incorporate many complicated devices. Moreover, we will use this chamber also at BL7U, a new beam line with a normal incidence monochromator connected with a planar undulator. Accordingly, the chamber was mounted on a micromotion stage in order to align its optical axis readily with the beam lines when the chamber is relocated.

Reference
1) A. T. J. B. Eppink and D. H. Parker, *Rev. Sci. Instrum.* **69**, 3477 (1997).
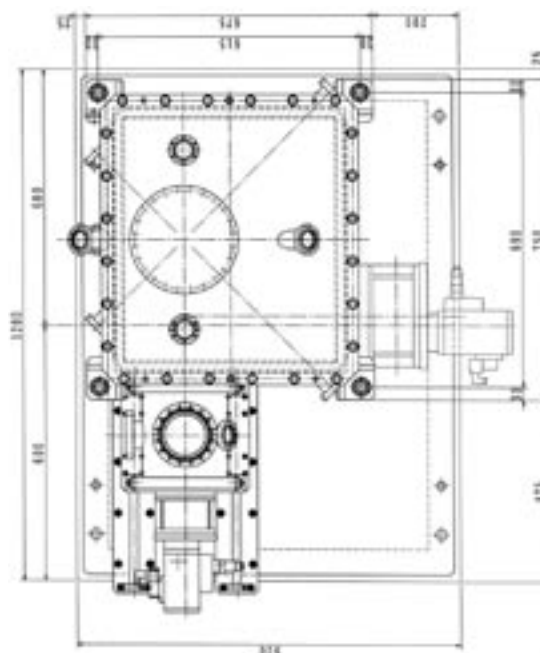
Figure 1. Drawing (top view) of the vacuum chamber on the micromotion stage (1200 × 900 mm) for the beam lines BL2B and BL7U in UVSOR.

VI-I Ray-Tracing for the Branch Beam Line of the 10-m Normal Incidence Monochromator Developed for Gas-Phase Photochemistry

Domestic synchrotron radiation facilities have no undulator beam line devoted to studies on gas-phase photochemistry in the vacuum ultraviolet (VUV) region. Kimura and coworkers in the UVSOR facility are constructing a new undulator beam line BL7U equipped with normal incidence monochromator, aiming at a maximum flux of 10^{11} photons/s (at 0.01% band width) and a maximum resolving power of 60000 [*e.g. UVSOR Activity Report* **2004**, 46 (2005)]. Our group is planning to construct a branch line to this monochromator. At the end station we will perform spectroscopic and dynamical studies of gas-phase molecules and clusters. Ray-tracing of the monochromator is in progress to determine the specifications of the branch line, with particular attention to the positions and shapes of post-focusing mirrors.

VI-I-1 Layout of the Branch Beam Line of BL7U

MITSUKE, Koichiro

The detailed design of the beam line 7U has been reported elsewhere,[1] so that we will briefly describe its layout (see Figure 1). The undulator is of APPLE-II type with a periodic length of 76 mm and the number of period of 38. Kimura and coworkers have adopted the normal incidence monochromator having an off-plane eagle mount in which three spherical gratings with 10-m focal length undergo translational and rotational motions. The undulator radiation is sampled by a pinhole, deflected horizontally at planar mirrors M0 and M1 by 10° and 165°, respectively, and made to irradiate the surface of one of the spherical gratings. The undulator radiation is further deflected horizontally at the grating by 182°. The dispersion plane of the grating lies vertically and the associated incidence and diffracted angles are always the same with varying from 0° (0th-order light) to 6° (the longest wavelength). The 1st-order light of the grating is deflected horizontally at the planar steering mirror M2 by 30° and focused onto the exit slit in the horizontal and vertical directions simultaneously. The light is then deflected horizontally at the toroidal postfocusing mirror M4 by 20°, thereby focusing onto the ionization point in the end station.

Reference
1) S. Kimura, *UVSOR Activity Report* **2004**, 46 (2005).
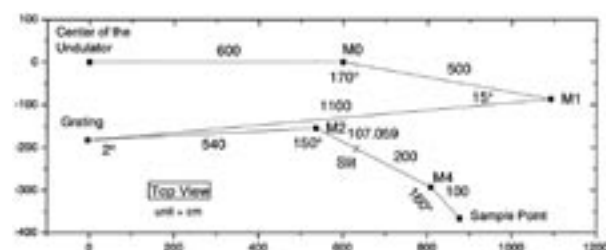
Figure 1. Layout of the beam line BL7U of UVSOR involving a 10-m normal incidence monochromator. The distances between two optical elements are in cm. Symbols Mn (0 ≤ n ≤ 4) designate the pre- and post-focusing mirrors.

VI-I-2 Ray-Tracing for the Branch Beam Line of BL7U of UVSOR

MITSUKE, Koichiro

The ray tracing is carried out at the fundamental of the undulator radiation around 17 eV at the deflection parameter of $K = 2.5$ by making use of the Shadow software. Panels a and b of Figure 1 show the spot images at the exit slit and ionization point, respectively, when 20000 rays ranging in the photon energy from 17.0497 to 17.0500 eV are generated randomly. We employed a grating with 2400 lines/mm, a slit with a 20 μm, and diffraction angle of 5.00695°. The sizes of the optical elements are taken into account, whereas their reflectivity and slope errors are neglected. The analysis showed that 6843 rays can arrive at the ionization point (Good rays) with a spot size of 20 μm × 400 μm. On the other hand, the number of the good rays is reduced to almost 3000, when the 20000 rays are generated in the photon energy range of either 17.0494–17.0497 eV or 17.0500–17.0503 eV. It is therefore likely that a resolving power of more than 30000 has been achieved. A resolving power of *ca.* 60000 is expected to be attained if we utilize a grating with 3600 lines/mm.
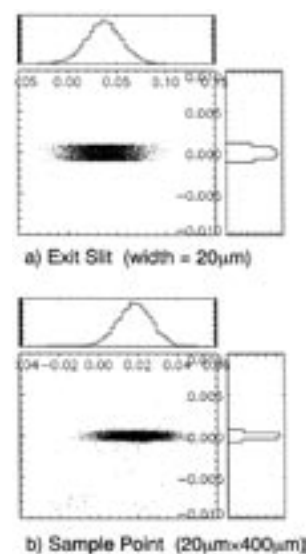
Figure 1. Spot images at the a) exit slit and b) ionization point under a 5-%-coupling operation.